Co@NH2-MIL-125(Ti): Cobaloxime-derived Metal-Organic Framework-based Composite for Light-driven H2 Production

Nasalevich, M.A.; Becker, R.; Ramos-Fernandez, E.V.; Castellanos, S.; Veber, S.L.; Fedin, M.V.; Kapteijn, F.; Reek, J.N.H.; van der Vlugt, J.I.; Gascon, J.

DOI
10.1039/c4ee02853h

Publication date
2015

Document Version
Final published version

Published in
Energy & Environmental Science

Energy & Environmental Science

PAPER

View Article Online
View Journal | View Issue

Cite this: *Energy Environ. Sci.*, 2015, **8**, 364

Co@NH_2-MIL-125(Ti): cobaloxime-derived metal–organic framework-based composite for light-driven H_2 production†

M. A. Nasalevich,‡[a] R. Becker,‡[b] E. V. Ramos-Fernandez,[c] S. Castellanos,[a] S. L. Veber,[d] M. V. Fedin,[d] F. Kapteijn,[a] J. N. H. Reek,*[b] J. I. van der Vlugt*[b] and J. Gascon*[a]

Received 8th September 2014
Accepted 17th November 2014

DOI: 10.1039/c4ee02853h

www.rsc.org/ees

We present a synthetic strategy for the efficient encapsulation of a derivative of a well-defined cobaloxime proton reduction catalyst within a photoresponsive metal–organic framework (**NH_2-MIL-125(Ti)**). The resulting hybrid system **Co@MOF** is demonstrated to be a robust heterogeneous composite material. Furthermore, **Co@MOF** is an efficient and fully recyclable noble metal-free catalyst system for light-driven hydrogen evolution from water under visible light illumination.

Broader context

The development of new strategies for the efficient valorization of solar light is one the most important challenges we face nowadays. Among the different possibilities, dihidrogen molecule is considered as one of the possible future energy carriers allowing for CO_2-free energy cycle. Although the photocatalytic water splitting was the first photocatalytic reaction to be discovered, no photocatalytic systems for this reaction have been industrially applied. This is both due to the fact that most discovered catalysts rely on the use of noble metals and to the low activities achieved so far by alternative catalysts. The application in this field of materials such as metal–organic frameworks (MOFs) can be a game changer in this research field. MOFs have been proven to be photoactive and their optical properties can be easily tuned towards visible light operation. The current challenge lies in the development of more appropriate active sites for the desired photocatalytic cycle. In this manuscript, we report a new strategy to achieve this goal. By introducing a derivative of the well-known molecular Co-based electrocatalyst Co-dioxime-diimine into the pores of a photo-active **NH_2-MIL-125(Ti)** following a 'Ship-in-a-bottle' strategy, we were able to synthesize a highly active photocatalyst composite free of noble metals, and fully recyclable. Because of the novelty and the implications of this work, we feel that it might appeal to the interdisciplinary readership of energy and environmental science. The journal has previously been an important forum for the research topics touched upon in this paper (new earth abundant materials and their application in (photo) catalysis and hydrogen evolution from water under visible light illumination). We would be glad to contribute to this discussion with one of the first examples of synergetic action between a MOF and a molecular catalyst for application in photocatalysis.

1. Introduction

The direct conversion of solar energy into chemical fuel is among the most important grand challenges today.[1] In analogy to natural photosynthesis, the best strategy to store solar energy is in chemical bonds of energy-dense molecules such as dihydrogen.[2] A technologically sound and scalable solar-driven H_2 production system from water requires not only robust functionalities for light-harvesting, charge transport, and catalysis and their efficient and durable interplay but also necessitates the use of earth-abundant elements and the assembly into practical devices.[3,4]

Recent advances in photocatalytic water splitting using earth-abundant composites – consisting of inorganic semiconductors and (organometallic) co-catalysts – have demonstrated the viability of designing complex assemblies. Moreover the overall reaction rate in such systems can often be influenced by tuning the individual constituents of the composite material.[5] Following this approach, the photocatalytic activity of TiO_2, firstly reported by Fujishima and Honda, has been greatly increased ever since.[6] Doping of the oxide with light elements such as nitrogen[7] as well as with metals[8] are among the most useful strategies. Dominant crystal facets and the lifetime of photogenerated charge carriers were recognized as key factors influencing the rates of photocatalytic reactions.[9,10] Another example of assembling a complex composite for H_2 production was recently reported by Qiao and co-workers. The system,

[a]*Catalysis Engineering, Applied Sciences, Delft University of Technology, Julianalaan 136, 2628 BL, Delft, The Netherlands. E-mail: j.gascon@tudelft.nl*

[b]*Homogeneous, Bioinspired and Supramolecular Catalysis, van't Hoff Institute for Molecular Sciences, University of Amsterdam, Science Park 904, 1098 XH, Amsterdam, The Netherlands. E-mail: j.i.vandervlugt@uva.nl; j.n.h.reek@uva.nl*

[c]*Laboratorio de Materiales Avanzados, Departamento de Química Inorgánica-Instituto Universitario de Materiales, Universidad de Alicante, Ap. 99, E-03080 Alicante, Spain*

[d]*Laboratory of Magnetic Resonance, International Tomography Center, Institutskaya 3A, Novosibirsk 630090, Russia*

† Electronic supplementary information (ESI) available: Experimental methods, spectroscopic and analytical data on catalyst and assembly characterization, photocatalysis and recycling results. This material is available free of charge *via* the internet at See DOI: 10.1039/c4ee02853h

‡ These authors contributed equally.

consisting of earth-abundant elements (Zn, Cd, Ni), afforded a quantum efficiency of around 30%.[11] Despite the impressive achievements in the field, photocatalysis with semiconductors remains challenging. Limited tuneability and the fact that photogenerated charges need to travel to the surface through the bulk semiconductors have to a large extent hindered further progress.

Metal–organic frameworks (MOFs) are ideal materials for the modular design of complex assemblies.[5,12,13] Distinct from traditional inorganic materials, MOFs can be reliably synthesized as extended hierarchical structures from well-defined molecular building blocks *via* crystal engineering.[14,15] MOFs have found application in organic photocatalysis, with the metal-containing nodes acting as semiconductor clusters spaced by photo-active organic struts.[12,16–21] Efficient photo-initiated strut-to-node electron-transfer has been demonstrated, although the reported photocatalytic activity cannot compete with traditional semiconductors.[22] Their performance can be enhanced by introduction of additional catalytic species, but these are commonly based on precious metals and the MOF typically only acts as container.[23–26]

To date, examples of cooperative action between a MOF matrix and encapsulated (molecular) catalysts are very scarce.[24,25,27–29] Inspired by natural photosynthesis, we envisioned a multi-component system that would allow for efficient photon-capture, charge-separation, electron-transport and catalytic turnover at different locations of a guest@MOF composite. This would offer efficient charge transfer between a stable, photo-active MOF structure and the encapsulated proton reduction catalyst under visible-light illumination. To achieve this overall modular design, the composite should contain (i) photoresponsive struts for fast light-harvesting, (ii) redox-active (multi) metallic nodes to allow charge-separation and accumulation of electrons and (iii) an appropriate MOF topology (*i.e.* large cavities connected by smaller windows) to encapsulate a molecular complex/nanocluster for productive turnover.

We herein demonstrate this principle with a cobaloxime-derived MOF-based (**Co@MOF**) system, consisting solely of earth-abundant elements. This material shows outstanding performance for several cycles without loss of activity in the light-driven hydrogen evolution from water under visible light illumination.

The synthetic protocol for assembling **Co@MOF** is described, followed by extensive characterization of the as-synthesized composite and the catalyst at work. However, a full comprehensive determination of the structure of this composite remains challenging. Commonly, the chemistry behind molecular cobalt complexes in solution and the ones embedded in rigid matrixes such as zeolites[30] is substantially different. Moreover, the lability of ligands constituting co-baloximes might cause coordination to the surrounding matrix resulting in cobalt species with different electronic properties.[31] Notwithstanding the aspects still to be unraveled, the remarkable performance of the MOF-based composite demonstrates the large application potential of the modular multifunctional design here presented.

2. Experimental

2.1. Materials and reagents

All chemicals were purchased from Sigma-Aldrich and Acros Organics and were used without further purification. Ligand $\mathbf{L^{H2}}$ (ref. 32) and cobaloxime (**1**)[33] were prepared according to modified literature procedures. Elemental analysis was performed by Kolbe Mikroanalytisches Laboratorium, Mülheim, Germany.

2.2. Syntheses

$\mathbf{L^{H2}}$ [$(DOH)_2$pn].

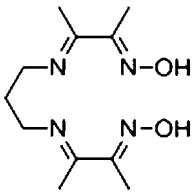

The crude ligand, N^2,$N^{2'}$-propanediylbis(2,3-butanedione 2-imine 3-oxime), was prepared using the method reported by Uhlig and Friedrich.[32] The resulting ligand was purified by repeated crystallizations from hot ethanol and washing with diethyl ether. This yields the pure ligand as a white solid, albeit in low yield (<10%). ^{1}H-NMR (400 MHz, DMSO-d6) δ 11.42 (s, 2H, N–OH), 3.46 (t, $J = 6.7$ Hz, 4H, CH_2), 1.98 (s, 6H, CH_3), 1.93 (qn, $J = 6.7$ Hz, 2H, CH_2), 1.91 (s, 6H, CH_3). Note that the quintet at 1.93 ppm is partially masked by the singlet at 1.91 ppm. MS-CSI for $C_{11}H_{20}N_4O_2$ ($(DOH)_2$pn): *m*/*z* calculated 241.16645, observed 241.16521 (M^+). Elemental analysis: found: C, 54.79; H, 8.35; N, 23.23. $C_{11}H_{20}N_4O_2$ requires C, 54.98; H, 8.39; N, 23.32%.

1 [$Co^{III}Br_2L^H$].

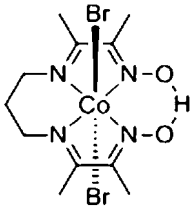

The crude complex was prepared using the method reported by Costa *et al.*[33] The resulting cobaloxime was purified by repeated crystallizations from ethyl acetate, yielding a green microcrystalline solid in 17% yield. ^{1}H-NMR (400 MHz, $CDCl_3$) δ 19.34 (s, 1H, OHO), 4.12 (t, 4H, CH_2), 2.65 (qn, 2H, CH_2), 2.61 (s, 6H, CH_3), 2.61 (s, 6H, CH_3). Note that the quintet at 2.65 and both singlets at 2.61 partially overlap. In the case of very impure product, the complex can be purified on Bio-Beads S-X8 (Bio-Rad) using THF as eluent. MS-CSI for $C_{13}H_{22}BrCoN_5O_2$ (CoBr-(MeCN) (DO) (DOH)pn): *m*/*z* calculated 418.0289, observed 418.0284 (M^+). Elemental analysis: found: C, 29.17; H, 4.20; N, 12.07. $C_{11}H_{19}Br_2CoN_4O_2$ requires C, 28.84; H, 4.18; N, 12.23.

MOF: NH_2-MIL-125(Ti) [$Ti_8O_8(OH)_4$-$(O_2C$–$C_6H_3NH_2$–$CO_2)_6$]. The synthesis of **NH_2-MIL-125(Ti)** was performed by dissolving 2.86 g (15.8 mmol) of 2-aminoterephthalic acid in a mixture of

40 mL of dry *N*,*N*-dimethylformamide (DMF) and 10 mL of dry methanol (at room temperature). Further 2.86 mL (9.7 mmol) of titanium isopropoxide was added and the mixture was placed in a Teflon liner inserted in a stainless steel autoclave. Then the autoclave was sealed and the mixture was heated for 72 hours at 110 °C. The obtained yellow solid was filtered and washed with DMF at room temperature. The as-synthesized solid was dispersed in DMF and kept under stirring overnight (50 mL of DMF per 1 g of product) in order to remove residual linker. Then, the same procedure was repeated twice using methanol instead of DMF to exchange the DMF within the pores. The solid was finally dried under air at 100 °C.

Co@MOF. 150 mg of **NH_2-MIL-125(Ti)** (90 μmol) was suspended in 40 mL of acetone and placed in a conical flask. Then 30 mg of $\mathbf{L^{H2}}$ (124 μmol) was added under continuous stirring. The ligand was allowed to adsorb overnight. The suspension was then centrifuged, washed gently with acetone once to remove the ligand adsorbed on the surface. After suspending the washed wet solid in 50 mL of fresh acetone, 120 mg of $CoBr_2 \cdot 6H_2O$ (367 μmol) was added under continuous stirring. The colour of the reaction mixture changes from yellow to green upon addition of $CoBr_2$. The suspension was stirred for 10 min and then a flow of air (30 mL min^{-1}) was applied for 10 min. Then the reaction was continued for 3 hours. The suspension was centrifuged and the product was washed with acetone 4 times to remove the residual $CoBr_2$. The solid was then washed with CH_3CN overnight, filtered off and dried at room temperature in air.

All the ratios listed above are given for the highest catalyst loading of 2.7 wt% of Co (as determined by ICP analysis).

Washing of catalysts. In order to wash the as-synthesized catalysts, the solids were subjected to conditions of hydrogen evolution but in the dark (no illumination): 300 mg of catalyst were suspended in a mixture of 300 mL of CH_3CN, 60 mL of triethylamine (TEA) and 6 mL of water in a 500 mL round bottom flask (ESI†). The mixture was deoxygenated with a flow of nitrogen for 30 min. The flask was then sealed, covered with aluminium foil and stirred overnight. 180 mL of acetone was added, stirred and the powder was filtered off. The powder was washed on a filter with acetone (2 × 500 mL) and dried in air.

2.3. Characterization and methods

Powder X-ray diffraction. Powder X-ray diffraction patterns were recorded using Bruker-AXS D5005 with CoKα radiation.

N_2-physisorption. N_2-physisorption experiments were carried out at 77 K in a Quantachrome Autosorb-6B unit gas adsorption analyser. Prior to the measurements the samples were degassed at 423 K under vacuum for 16 hours. The BET surface areas were calculated using intervals allowing positive BET constants. The total pore volumes were calculated at 0.9 relative pressure.

High resolution TEM. High resolution TEM was performed using a FEI Tecnai TF20 electron microscope with a field emission gun as the source of electrons operated at 200 kV. Samples were mounted on Quantifoil® carbon polymer supported on a copper grid by placing a few droplets of a suspension of ground sample in ethanol on the grid, followed by drying at ambient conditions.

Energy-dispersive X-ray spectroscopy (TEM). Energy-dispersive X-ray spectroscopy (TEM) elemental analysis was performed using an Oxford Instruments EDX system. The copper signal in the EDX spectra is due to background radiation hitting the copper sample holder grid.

For all samples, many digital images were recorded, and all useful images have been transferred *via* ftp.

Scanning electron microscopy (SEM). Scanning electron microscopy (SEM) was carried out using a JEOL JSM-6010LA InTouchScope microscope equipped with an integrated SDD EDS detector.

Infrared Spectroscopy. Infrared Spectroscopy was carried out using a Thermo Nicolet Nexus FTIR spectrometer. The samples (5 mg) were mixed with KBr and pressed into self-supported pellets (50 mg cm^{-2}). The spectra were taken in the transmission mode in an *in situ* cell equipped with CaF_2 windows. Prior to the measurements, the samples were degassed in vacuum (10^{-5} mbar) at 423 K for 2 hours to remove adsorbed molecules.

Diffuse reflectance UV/vis. Diffuse reflectance UV/vis spectra were collected using a Perkin–Elmer Lambda 900 spectrophotometer equipped with an integrating sphere ("Labsphere") in the 200–800 nm range. $BaSO_4$ was used as a white standard.

Transmittance UV/vis. Transmittance UV/vis spectra were measured with a Perkin–Elmer Lambda 40 spectrophotometer. Liquid samples were studied in Hellma 110-QS cuvettes with 1 mm optical path length.

Photoluminescence. Steady-state emission spectra were acquired using a QuantaMaster QM-1 (PTI). 100 W Xenon arc lamp (200–900 nm) was used as a light source equipped with 121A excitation double monochromators. Model MP-1 sample compartment, 101A emission monochromator, model 710 photon counting detector PMT (185–900 nm) completed the experimental setup. The experiments were carried out in solid state. The slit in all measurements was 10 nm. Fluorescence lifetime measurements were carried out using a LifeSpec-ps by Edinburgh Instruments equipped with a 405 nm laser diode. The laser pulse was 80 ps. The lifetimes were acquired using standard 1 cm optical path length cuvettes. The experiments were performed on suspensions of 1 mg of a solid in 10 mL of CH_3CN. The samples denoted 'N_2' were additionally deoxygenated in a cuvette by purging a flow of nitrogen through the suspension for 2 min.

EPR spectroscopy. Steady-state EPR measurements were carried out at X-band (9 GHz) using a commercial EPR spectrometer Bruker Elexsys E580 equipped with an Oxford Instruments temperature control system (T = 4–300 K). All spectra were acquired at 40 K. Samples were prepared by suspending pristine **NH_2-MIL-125(Ti)** or **Co@MOF** in a solution of electron donor TEA/CH_3CN/H_2O. The volume of suspension placed into the EPR resonator was 50–60 μL. Each sample was degassed by several freeze–pump–thaw procedures and then sealed. When needed, the samples were exposed to >420 nm visible light irradiation.

NMR spectroscopy. All spectra were recorded on a Bruker ARX400. Chemical shift values were corrected with respect to the solvent residual signal (DMSO-d_6: 2.50, $CDCl_3$: 7.26, D_2O: 4.79). For the digestion of solid catalysts 30 mg of a powdered sample was suspended in 0.3 mL of 40% NaOD solution and heated overnight at 60 °C under continuous stirring. After cooling down to room temperature, the paste-like mixture was neutralized with DCl (around 0.3 mL) and centrifuged. The aqueous later is then subjected to ^{1}H-NMR (further denoted as aqueous) while the precipitate is extracted once with 0.3 mL of DMSO-d_6 and the organic phase is analysed (further denoted as Organic).

Mass-spectrometry. Mass-spectrometry was performed on a Time-of-Flight JEOL AccuTOF LC-plus mass spectrometer (JMS-T100LP) equipped with a cold spray ionization source (CSI). Calculated spectra were obtained with JEOL Isotopic Simulator (version 1.3.0.0).

Experiments with D_2O. A typical photocatalytic reaction was performed using the procedure stated in paragraph 2.4, except that D_2O (99.9 atom% D; fresh bottle) was used instead of H_2O. After 10 hours of irradiation, part of the reactor's head space was collected using a 5 mL gas-tight syringe and injected through a septum in the MS and the signals $m/z = 2$ and $m/z = 4$ were monitored. Mass spectrometry (MS) analysis of the gases was performed using a Pfeiffer QMS 200 mass spectrometer. The mass spectrometer was connected to a manifold that continuously supplies Ar (50 mL min^{-1}) to the inlet part of the MS.

Using a pure D_2 sample, it was confirmed that D_2 only gives rise to ion current for $m/z = 4$ and does not fragment to $m/z = 2$.

2.4. Photocatalysis

In a typical experiment, **Co@MOF** (5.0 ± 0.2 mg) was suspended in a mixture of acetonitrile (5 mL), triethylamine (1 mL) and deionized water (100 μL) and the suspension degassed by bubbling nitrogen for 10 min while stirring. The resulting suspension was transferred (under nitrogen atmosphere) to a photo-reactor (head space approximately 200 mL) which was purged with nitrogen beforehand. The sample was irradiated continuously with a 500 W Hg/Xe lamp (Hamamatsu Photonics L8288) at the lamp's focal point (*ca.* 45 cm) using an IR filter (circulating water; *ca.* 25 cm path length) and a 408 nm UV cut-off filter. The head space was sampled continuously (every 10 min; 20 μL sample volume) by online gas chromatography (Interscience CompactGC; molecular sieve column, Ar carrier, TCD detector) using internal calibration against the dinitrogen peak.

2.5. Recycling

After irradiation, the reaction mixture was transferred to a centrifuge tube and diluted with acetone (5 mL). The suspension was centrifuged at 4000 rpm for 20 min and the supernatant (including some fine catalyst particles) was discarded. The solid residue was subjected to a gentle acetone wash (10 mL) and again centrifuged (twice). The final solids were air dried, and used in the next photocatalytic run 'as is'. Note that during recycling, traces of material are most probably lost as fine particles in the mother liquor. Quantification of the recovered material was not possible due to the small sample mass and presence of solvent traces, but the yield seemed to be quantitative.

3. Results

In this work we aimed at encapsulating the well-defined molecular electrocatalyst (**1**) within the cavities of a photoactive MOF, namely **NH_2-MIL-125(Ti)**. For this purpose we designed a two-stage 'ship-in-the-bottle' strategy (Scheme 1). Firstly, the pores of the MOF structure are loaded with the flexible organic component $(DOH)_2pn$ ($\mathbf{L^{H2}}$), where after addition of $CoBr_2$ under aerobic conditions should lead to assembly of complex **1** within the large cavities of the metal–organic framework. The size-selectivity principle is key to this intra-MOF complex synthesis, as the dimensions of the intact Co^{III} pre-catalyst exclude diffusion into or out of the MOF windows as confirmed by control experiments summarized in Fig. S6.†[34]

The resulting catalysts were extensively characterized and their performance in visible light-driven hydrogen evolution was evaluated. In this section the experimental results are reported, followed by the discussion in the next section. We emphasize the discrimination between the two since the numerous characterization techniques employed in this study suggest the formation of the designed photocatalytic composite **Co@MOF** but do not comprehensively prove the exact configuration of the molecular species of cobalt within the pores of the MOF.

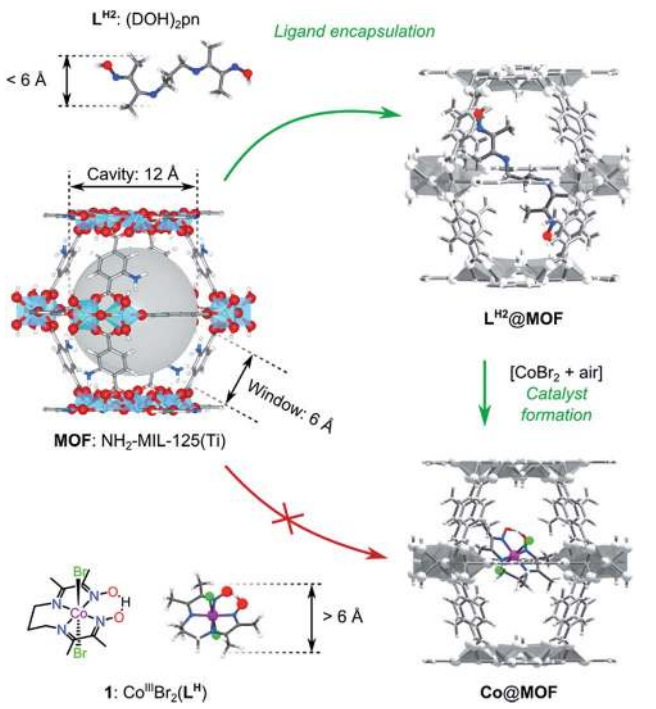

Scheme 1 'Ship-in-a-bottle' synthetic strategy followed for assembling of Co@MOF.

3.1. Catalysts characterization

ICP-MS. The loading of cobaloxime was varied by scaling the amount of ligand and $CoBr_2$ simultaneously to obtain **Co@MOF** with an average amount of catalyst molecules per cavity as listed below (Table 1).

ICP analysis confirms the inclusion of Co-containing species into the MOF with the total cobalt content in a range of 1.1–2.7 wt%.

N_2-physisorption. N_2 physisorption experiments revealed an expected drop of the total pore volume in the case of **Co@MOF** bearing the highest cobalt content as compared to the pristine **NH_2-MIL-125(Ti)**. Fig. 1 displays nitrogen isotherms of the two catalysts.

The pristine **NH_2-MIL-125(Ti)** displays a total pore volume of 0.58 $cm^3\ g^{-1}$, in line with previous reports,[35] while the **Co@MOF** shows a significantly lower N_2-uptake, resulting in a total pore volume of 0.46 $cm^3\ g^{-1}$. At the same time, the solid remains microporous and preserves a significant fraction of the pore volume. This indicates that the cobalt species formed by the synthetic two-stage procedure do not block the pores of the framework and are likely to be of molecular size due to the size restrictions by the cavities of the MOF.

Transmission Electron Microscopy. The TEM micrographs of pristine **NH_2-MIL-125(Ti)** and **Co@MOF** are depicted in Fig. 2:

The pristine MOF consists of well-defined crystallites with a diameter of approximately 400 nm. The **Co@MOF** crystallites are nearly identical to the ones of the MOF with no agglomerates nor core/shell type structure found by TEM. In fact, the cobalt entities within the MOF crystallites could not be distinguished by this technique implying that the size of the cobalt species is not exceeding 2 nm. EDX analysis performed on multiple regions in Fig. 2D shows nearly the same cobalt content on the surface of the crystallite and in the bulk [Table S1†]. Moreover, SEM EDX mapping on μm scale demonstrated the absence of large agglomerates of Co or Ti and confirmed the homogeneity of the composite (Fig. S12†). These observations support the hypothesis that the cobalt species is molecularly dispersed within the MOF cavities, in line with the nitrogen physisorption results.

Powder X-ray diffraction. Fig. 3 shows PXRD patterns of the MOF and **Co@MOF**. The crystal structure of **NH_2-MIL-125(Ti)** remains intact upon assembly of cobalt complex. The PXRD pattern of **Co@MOF** does not contain any additional Bragg peaks. In both cases the most dominant Bragg reflection was found to be the one corresponding to (101) crystal facet.

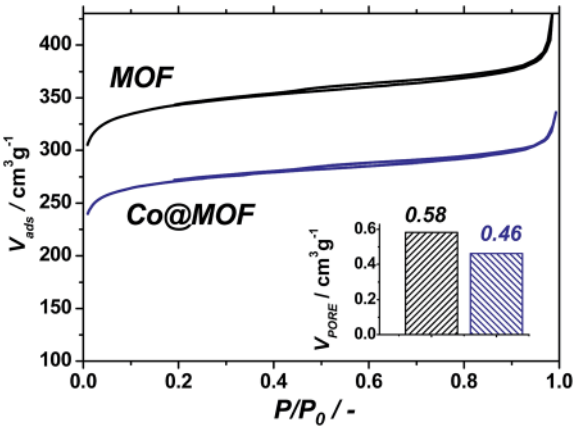

Fig. 1 Nitrogen isotherms recorded at 77 K for pristine NH_2-MIL-125(Ti) (black) and Co@MOF (blue). Total pore volumes calculated at 0.9 P/P_0 (bottom right).

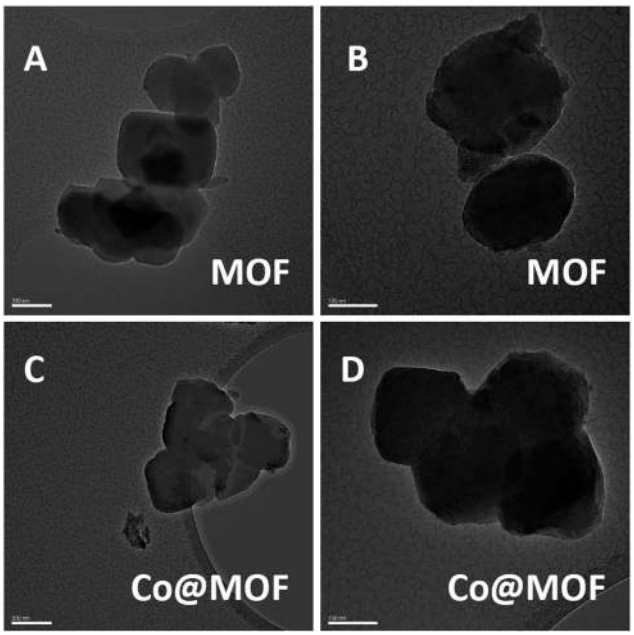

Fig. 2 TEM of pristine NH_2-MIL-125(Ti) (200 nm – A; 100 nm – B) and Co@MOF (200 nm – C; 100 nm – D).

Table 1 ICP analyses of the catalysts synthesized in this work

Sample	Co/w% by ICP	Catalyst:cavity[a]	Comment
NH_2-MIL-125(Ti)	0	0	Pristine MOF
Co@MOF-1	1.1	0.343	
Co@MOF-2	2.0	0.675	
Co@MOF-3	2.2	0.756	
Co@MOF-4	2.7	0.973	

[a] The number of catalyst molecules per cavity was based on the Co : Ti ratio of 1 : 8.

Infrared spectroscopy. Infrared spectroscopic studies performed on the **Co@MOF** *vs.* the pristine MOF do not reveal the signatures characteristic for cobaloxime,[1] likely because the **NH_2-MIL-125(Ti)** signals dominate both the fingerprint and the group-frequency regions (Fig. 4), however an observed red shift of the bands associated to the amino-groups of the MOF and an increase in the alkyl region suggest the inclusion of the cobalt complex in the cavities of the scaffold. The symmetric and assymetric NH_2 stretching of pristine **NH_2-MIL-125(Ti)** are found at 3521 and 3394 cm^{-1} respectively, while in the case of **Co@MOF** composite they are shifted to 3509 and 3380 cm^{-1}.

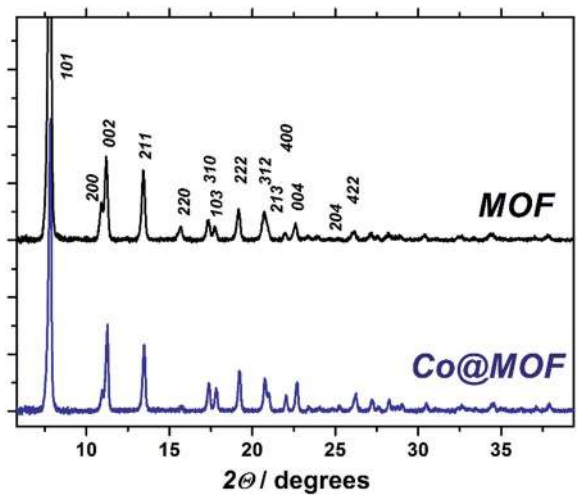

Fig. 3 Powder X-ray diffraction patterns of pristine NH_2-MIL-125(Ti) (black) and **Co@MOF** (blue). Vertical numbers denote corresponding crystal facets.

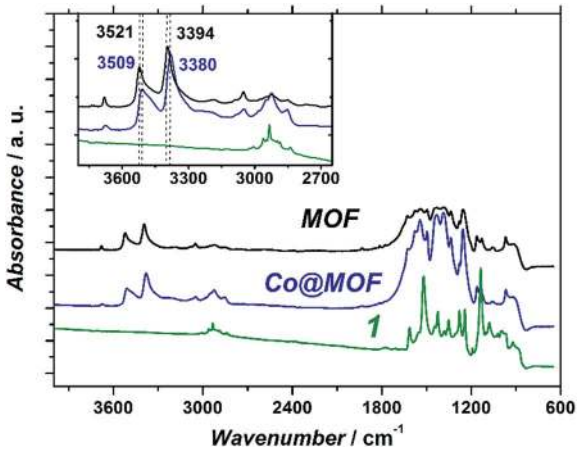

Fig. 4 Infrared transmittance spectra of pristine NH_2-MIL-125(Ti) (black), **Co@MOF** (blue) and **1** (green).

Diffuse reflectance UV/Vis spectroscopy. UV/Vis spectra **1**, MOF and **Co@MOF** collected in reflectance mode and Kubelka–Munk representation are shown in Fig. 5:

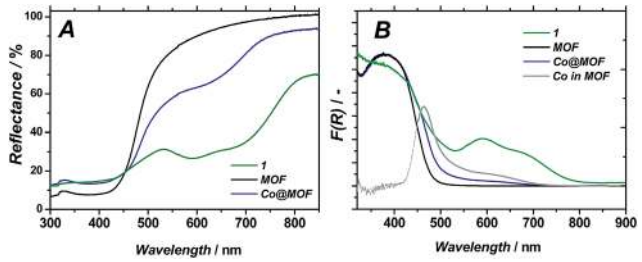

Fig. 5 Diffuse reflectance UV/Vis spectra of **1**, pristine MOF and **Co@MOF** (A); Kubelka–Munk representation (B); 'Co in MOF' curve is obtained by subtracting MOF from **Co@MOF**.

UV/Vis spectroscopy on **Co@MOF** catalyst showed the appearance of two new features at 440 and 585 nm (see Fig. 5B) as compared to the pristine framework, which are ascribed to the inclusion of complex **1** (maxima at 400 and 600 nm).[36] The major optical absorption of **1** is found at around 400 nm. However, this absorption band of **1** is masked in **Co@MOF** by the n–π* transition of **NH_2-MIL-125(Ti)** that corresponds to a HOMO-LUMO gap energy of 2.73 eV. It should be emphasized that the intense longer wavelength transitions[36] characteristic for Co^{2+} species were not observed in **Co@MOF**. The spectrum is attributed to be the result of a combination of individual absorption spectra from **NH_2-MIL-125(Ti)** and **1**. Thus the newly appeared intense band allows for the estimation of the HOMO-LUMO gap of the **1**-derived entities encapsulated in the MOF (2.59 eV, Fig. S8†), while the gap of the NH_2-MIL-125 is assumed to be equal to the pristine MOF.

Photoluminescence spectroscopy. Steady-state emission spectra of **1**, **Co@MOF** and pristine MOF were acquired in solid state. The samples were excited at the wavelengths corresponding to their absorption maxima.

As can be seen in Fig. 6B, the pristine **NH_2-MIL-125(Ti)** displays one single emission band centred at 433 nm, in line with the previously reported data.[37] In case of pristine **1**, photoemission does not occur upon excitation at 590 nm, in spite of the absorption band at this wavelength shown in Fig. 5B, corresponding to weak oscillator strength optical transitions of the cobaloxime. In contrast, excitation at 380 nm yields an intense well-defined emission band centred at 435 nm matching the emission of the as-prepared MOF. **Co@MOF** demonstrates emissions markedly different from the ones found for **NH_2-MIL-125(Ti)**. The broad emission band has now two distinct components centred at 418 and 437 nm. We speculate that the following assignments are possible: (i) blue-shifted emission of **1** confined in the MOF environment at 418 nm and unperturbed emission of **NH_2-MIL-125(Ti)** at 437 nm; (ii) blue-shifted emission of the MOF interacting with **1** and unperturbed emission of **1**; (iii) two different emitting entities within the MOF: one interacting with **1** and the other unperturbed. Fluorescence lifetimes of the excited states for **NH_2-MIL-125(Ti)** and **Co@MOF** were also investigated. Characteristic decay time was found to be 11.3 ns in the case of the MOF while it was 11.6 ns for **Co@MOF** system. The same experiments carried out in deoxygenated CH_3CN suspension showed elongation of both lifetimes that became 16.5 ns (Fig. S9†).

NMR of digested solids. To gain further insight in the structure of the cobalt species within the pores of the framework, **Co@MOF** catalyst was subjected to digestion under basic conditions followed by neutralization and extraction with DMSO. The spectrum of the aqueous phase resulting from the **Co@MOF** digestion displays a doublet : doublet : singlet (1 : 1 : 1) multiplicity at 8.34, 8.24 and 8.21 ppm, respectively, arising from the amino-terephthalate aromatic linker (Fig. S3†). Most remarkably, and contrary to the case of the pure MOF, additional signals in the aliphatic region were also detected. A comparable overlapping of signals in the same window range was observed after performing the same digestion procedure on the cobaloxime complex (Fig. S4†). Thus, although an

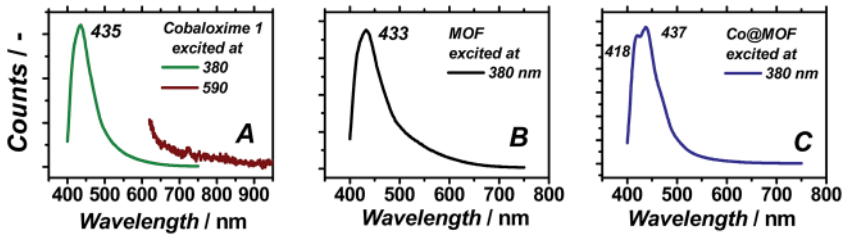

Fig. 6 Steady-state photoluminescence spectra of **1** (A), MOF (B) and **Co@MOF** (C).

unequivocal assignment cannot be ventured, this result is in agreement with the presence of extra organic residues originating from the cobaloxime moiety in the **Co@MOF** sample.

3.2. Photocatalytic performance

In order to assess the ability of **Co@MOF** to perform light-driven hydrogen evolution, the catalyst was suspended in a mixture of acetonitrile, triethylamine and water (5 : 1 : 0.1 v/v), deoxygenated and exposed to visible-light illumination. Online-GC monitoring of the composition of the head space of the reactor enabled assessment of the catalytic performance of pristine MOF and **Co@MOF** catalyst (Fig. 7A). Results obtained for catalysts bearing different Co loadings are depicted in Fig. 7B.

When cobaloxime alone is used as homogeneous catalyst, no hydrogen evolution is observed. Indeed, catalyst **1** is known to be an excellent electrocatalyst, but cannot act as photocatalyst in the absence of a separate photo-sensitizer.[38] In agreement with previous reports, pristine **NH_2-MIL-125(Ti)** was confirmed to produce only a moderate amount of hydrogen gas.[24] The novel assembly system **Co@MOF** showed markedly improved photocatalytic performance, with up to 20-fold higher H_2 production rate compared to pristine cobalt-free MOF. More importantly, **Co@MOF** maintains a constant TOF of 0.8 h^{-1} even after 65 hours of total operation, indicating a high stability under illumination conditions. Moreover, similar TOFs (per Co atom) are obtained for catalysts bearing different amounts of cobalt entities, even for catalysts containing up to one cobalt atom per MOF cavity, demonstrating the absence of diffusion limitations and efficient charge transfer even at relatively high loadings. Additional kinetic experiments demonstrate that, once the stepwise assembly of **Co@MOF** is completed, no leaching of Co occurs from the composite (Fig. 7C); the system could be recycled several times without any loss of activity and with no remaining catalytic activity in solution after filtration of the catalyst. The external quantum efficiency (EQE) of the best performing **Co@MOF** catalyst (2.7 w% Co) was found to be *ca.* 0.5% (ESI†). The calculated apparent activation energy for hydrogen production using **Co@MOF** was 0.4 eV (ESI†).

3.3. Proton source for hydrogen evolution

When D_2O was employed as a reactant, significant amounts of D_2 were observed ($H_2/D_2 \approx 1$), evidencing the participation of water in the formation of hydrogen gas (Fig. 8A). In the present system, the formed triethylamine radical cation has a pK_a comparable to water,[39] and additional formation of H_2 through proton exchange between the two species seems reasonable.

3.4. Mechanistic aspects of hydrogen evolution catalysed by Co@MOF assessed by EPR

Quasi in situ EPR experiments on **Co@MOF** and pristine **NH_2-MIL-125(Ti)** at 40 K after illuminating at room temperature in the presence of an electron-donor indicate efficient charge transfer from the MOF to the cobalt species within the composite.[40] Continuous wave (CW) EPR spectra of **NH_2-MIL-125(Ti)** and **Co@MOF** were recorded at X-band microwave frequency (9.55 GHz). Fig. 8B displays CW EPR spectra of pristine **NH_2-MIL-125(Ti)** in the dark and after 30 min of visible light illumination.

An intense EPR signal centred at $g = 1.94$ evolved upon irradiation, which was attributed to paramagnetic Ti^{III} formed by ligand-to-metal charge transfer (LMCT).[24,25] The small

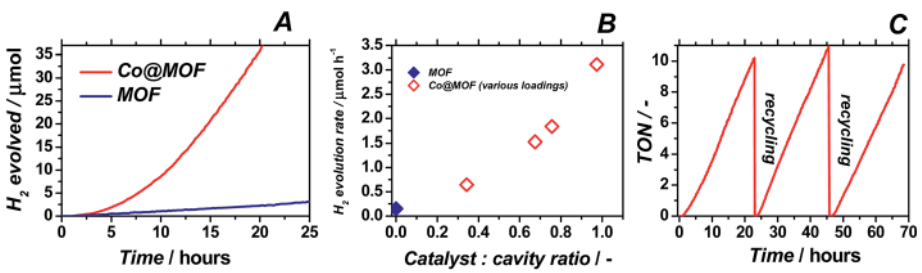

Fig. 7 (A) Photocatalytic proton reduction using MOF and **Co@MOF**. (B) Steady state H_2 evolution rate plotted against the average number of cobalt atoms inside each MOF cavity. (C) Recycling tests on **Co@MOF** bearing medium cobalt loading. Conditions: 5 mg catalyst, 5 mL CH_3CN, 1 mL TEA, 0.1 mL H_2O, 500 W Xe/Hg lamp using $\lambda > 408$ nm.

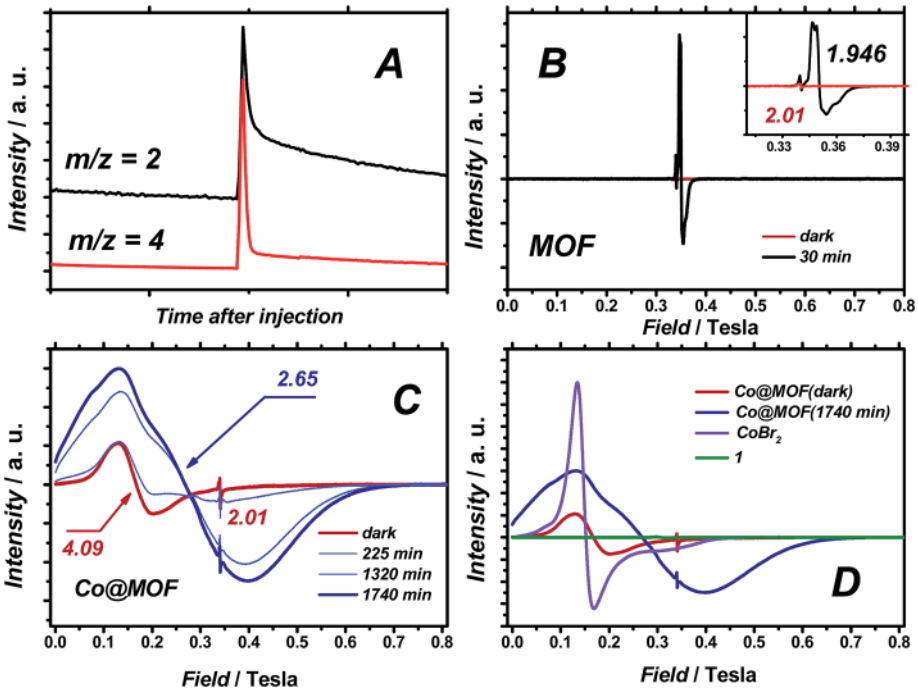

Fig. 8 (A) MS analysis of the products formed when using D_2O, (B) CW EPR spectra of pristine MOF in the dark and upon irradiation, (C) **Co@MOF** in the dark and upon irradiation, (D) comparison with reference compounds.

downfield feature at $g = 2.01$ is associated with the spatially confined amino-groups in the MOF.[26,41] The EPR spectrum of **Co@MOF** in the dark (Fig. 8C), with a broad signal around $g \approx 4$, is similar to that of high-spin $CoBr_2$ in CH_3CN, indicating the presence of residual high-spin Co^{II} impurities (Fig. 8D). The major fraction of cobalt is believed to be in the stable low-spin diamagnetic Co^{III} state. Exposing **Co@MOF** to visible light for 22 hours results in the gradual rise of a new broad and intense line, significantly upfield-shifted with respect to $CoBr_2$ admixtures. Quantitative analysis of the EPR data shows a ten-fold higher integral intensity for this paramagnetic signal after illumination compared to the 'dark' sample. This photoinduced EPR signal, simulated using reasonable effective g-tensor $g_x = 6.0$, $g_y = 2.4$, $g_z = 1.7$, can be assigned to the high-spin Co^{II} species (ESI†).[42] Importantly, contrary to the pristine MOF sample, no EPR signal was detected for a Ti^{III} species in **Co@MOF**, demonstrating the efficient charge transfer between the photogenerated charge-separated state in the MOF and **1**-derived species.

4. Discussion

The two-stage 'ship-in-a-bottle' synthetic protocol followed in this study resulted in the synthesis of a **Co@MOF** photocatalytic composite: a catalyst free of noble metals, recyclable and displaying a stable TOF of 0.8 h^{-1} even after 65 hours of operation. The introduction of the cobaloxime-derived active sites into the cavities of the framework resulted in a 20-fold enhanced photocatalytic activity compared to the pristine **NH_2-MIL-125(Ti)** used as a benchmark. Importantly, the catalyst utilizes water as a source of protons. With all these characteristics, the present composite outperforms every MOF-based analogue reported so far in literature (ESI†). Having said this, the actual structure of the Co species in the composite and the exact mechanism behind its remarkable performance are still unclear. In the following section these aspects are discussed in detail.

4.1. Modular design

NH_2-MIL-125(Ti) was selected as host material because (i) the overall MOF structure is stable in aqueous media,[43,44] (ii) the multinuclear Ti-centers are both photo- and redox-active[24,45] and (iii) recent experimental[37] and theoretical studies[46] have shown that the photochemical properties can be tuned by changing the aromatic linker. It is noteworthy that **NH_2-MIL-125(Ti)** has been used for photocatalytic hydrogen production, both in the absence and presence of Pt-nanoparticles,[24] suggesting that the reduction potential of the excited states in the MOF is sufficient to drive proton reduction in line with computational predictions.[47] We chose the oxygen-tolerant and readily synthesized cobalt complex **1** $Co^{III}Br_2(L^H)$ (L^H = (DO)(DOH)pn), previously employed as electrocatalyst for proton reduction,[48,49] as molecular guest to demonstrate our concept[50,51] illustrated in Scheme 2:

4.2. Role of cobalt active sites

First of all, the importance of cobalt as an additional catalytic site should be underlined. From the catalytic experiments displayed in Fig. 7B it is evident that the rate of the photo-assisted transformation increases with higher cobalt loading. Importantly, the injection of a deoxygenated solution of $CoBr_2$ into the

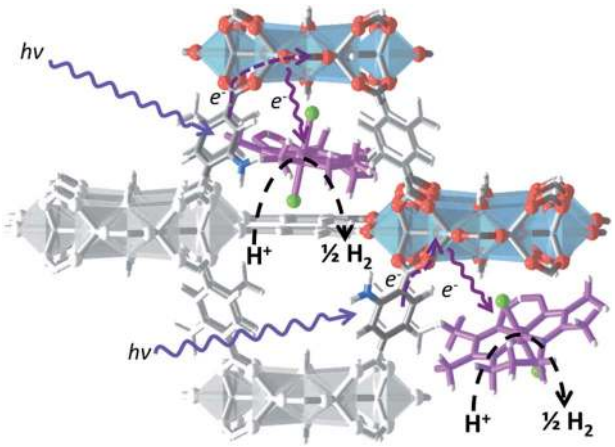

Scheme 2 Concept of photocatalytic H_2 production using a multi-functional MOF-based composite.

working catalyst suspension immediately suppressed the activity of the composite as shown in Fig. S16.† The composite was subjected to 70 hours of reaction to ensure the stable operation before the $CoBr_2$ was injected. Similar observations were reported by Marassi and co-workers, who found that the first step in electrocatalytic hydrogen formation catalysed by **1** is the displacement of the axial bromido ligands.[52] This dissociative process is at equilibrium and can be shifted towards the six-fold coordinated complex upon the addition of Br-ions. Moreover, our experiments with $CoBr_2$ injection emphasize the importance of using the ligand $\mathbf{L^{H2}}$ [$(DOH)_2$pn] as a precursor for the assembly of the catalytically active composite. In order to further confirm the key role of the $\mathbf{L^{H2}}$ ligand, we prepared an additional composite by exposing the pristine MOF to the same synthetic conditions as for the **Co@MOF** assembly except that no ligand was added to the suspension or previously encapsulated in the MOF system. The resulting composite was subjected to UV/Vis spectroscopy and photocatalytic tests. The resulting material entitled **$CoBr_2$@MOF** produced no hydrogen after 24 hours of irradiation. Moreover, the absorption spectrum of the material is substantially different from the one of **Co@MOF**, as illustrated in Fig. S7.† These control experiments prove the necessity of employing the organic ligand for the assembly of a photocatalytically active **Co@MOF** composite. We should mention that inhibition of the photocatalytic reactions by introducing Br was observed for both the MOF and **Co@MOF**. These results imply that besides the suppressed dissociation of the reduced cobaloxime **1**, bromides are likely to inhibit the catalysis by **NH_2-MIL-125(Ti)** due to the catalyst poisoning.[53] For **Co@MOF** composite either of the scenarios is possible.

Introduction of the additional catalytic sites into **NH_2-MIL-125(Ti)** increased the activity by a factor of 20, resulting in EQE of 0.5% for **Co@MOF** composite. With this performance the present catalyst compares well with a system reported by Reisner and colleagues.[54] This system comprised of nanosized TiO_2, Ru-based dye as a photosensitizer and cobaloxime as a catalytic site produced hydrogen at EQE of 1%.[55] The advantage of **Co@MOF** composite is the absence of noble metals however, the catalyst yet exhibits moderate efficiencies when compared against state of the art semiconductor-based systems.[56,57]

4.3. Molecular cobalt catalyst

Transmission electron microscopy and energy-dispersive X-ray spectroscopy measurements indicate that cobalt species are likely to be of molecular size and homogeneously distributed over the composite crystallites. These observations are also supported by nitrogen physisorption results that indicate that the significant fraction of the pore volume of the pristine **NH_2-MIL-125(Ti)** is preserved upon forming the **Co@MOF**.

4.4. Structural features of organometallic cobalt species

Nuclear magnetic resonance experiments on the digested **1**, MOF and **Co@MOF** confirmed the presence of residual organic species likely originating from the $\mathbf{L^{H2}}$ [$(DOH)_2$pn] ligand. Although the full assignment of the observed signals is beyond the scope of this work, it is evident that they can not be attributed to the pristine MOF nor to the solvents used for the synthesis of **Co@MOF**, CH_3CN and acetone. Triethylamine found in the digested composite was used for the activation protocol described in the experimental part. Moreover, the

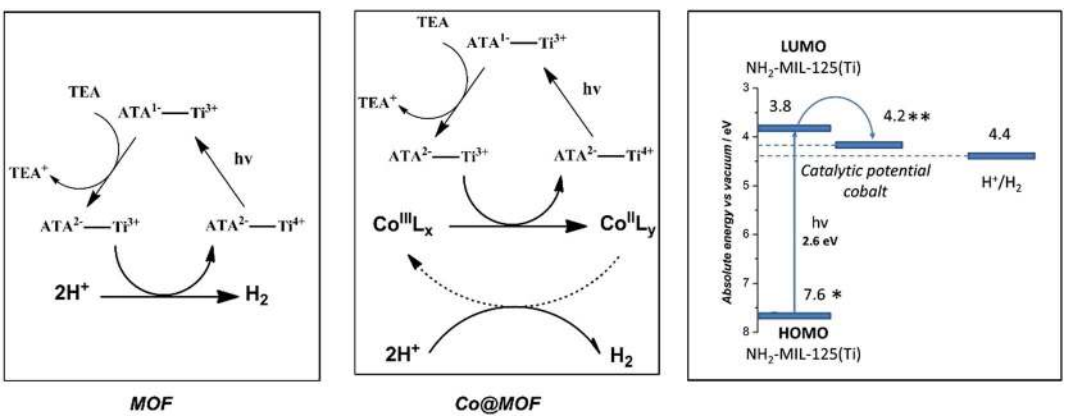

Scheme 3 Proposed hydrogen evolution mechanisms in pristine MOF (left) and Co@MOF (centre). ATA = 2-aminoterephthalic acid. Schematic diagram of redox potentials of components of Co@MOF composite (right). (*): Calculated values. (**): Experimental data.

similarities found between the spectra of digested **1** and **Co@MOF** suggest the successful assembly of the complex within the MOF cavities.

UV/Vis spectroscopy together with luminescence studies support the formation of the proposed cobalt structure within the cavities of the framework. Upon subtraction of the absorption spectrum of MOF from that of **Co@MOF** (Fig. 5B) an absorption band of the newly formed species becomes apparent below 440 nm. The longer wavelength absorption at around 600 nm is broadened and poorly defined. Luminescence spectroscopy carried out on **Co@MOF** demonstrates that, compared to the pristine **NH_2-MIL-125(Ti)**, the cobalt containing solid clearly emits at two different wavelengths upon excitation at 380 nm. All together, these results point at the inclusion of species with the main absorption band around 400 nm, weak oscillator strength transition at around 600 nm and the emission band located at 418 or 437 nm. These characteristic absorption bands are typical for **1**, as reported by Reisner and co-workers.[36]

The fact that the **Co@MOF** catalyst can be recycled multiple times and that no activity arises from the filtrate after isolating the solid confirms that the composite is purely heterogeneous. Noteworthy, both the cobalt precursor, $CoBr_2$ and cobaloxime **1** are soluble at the conditions of the photocatalytic reaction. These data, together with the molecular nature of the cobalt species, imply that the cobalt active sites within **Co@MOF** are either encapsulated on the basis of the size-selectivity principle or bound to the MOF matrix. The two most likely sites in the MOF structure for coordinating the cobalt centre are the bridging OH-groups within the titanium oxoclusters and the NH_2-groups of the organic linkers. The observed shift of amino-stretchings of the framework could indicate such interactions, however a more detailed investigation of these phenomena is needed. Furthermore, EPR analysis of the photoinduced Co^{II} species within **Co@MOF** reveals a distorted geometry of the high-spin cobalt complex. This spin-state can be explained by: (i) coordination to weak field ligands such as NH_2 and/or (ii) distortion of the geometry of the complex confined in the MOF matrix. These observations also support the hypothesis of guest–framework interactions.

Electron paramagnetic resonance experiments on **Co@MOF** in the dark revealed that the main fraction of cobalt in the catalyst is in its EPR-silent Co^{III} state that is converted to high-spin Co^{II} species upon illumination. Compared to high-spin $CoBr_2$ (Fig. 7D) that exhibits Lorentzian line broadening and can be described by effective axial $g_x = g_y = 4.8$, $g_z = 2.0$ (ESI†), the photoinduced Co^{II} species have lower symmetry and overwhelmingly Gaussian line shape. Both observations imply that a confinement in the MOF affects the geometry/composition of Co^{II} complex and leads to a conformational distribution that requires a more detailed investigation in the future. Moreover, the EPR spectrum of **Co@MOF** after illumination is markedly different from that of reduced **1** (by reaction with cobaltocene) found in low-spin state evidenced by well-defined hyperfine coupling (Fig. S22†). These findings point towards differences between the MOF-free molecular catalyst **1** and cobalt species found within the **Co@MOF** composite. Most importantly, the resonance signal of Ti^{3+} found in the excited pristine **NH_2-MIL-125(Ti)** is not found in the case of **Co@MOF** proving the successful electron transfer between the different components of the composite.

4.5. Proposed mechanism

On the basis of the EPR observations we speculate that the photoexcited state of the MOF is generated *via* the following mechanism: upon photon-absorption by the MOF linker, charge separation takes place to generate Ti^{3+} and a hole at the organic linker. The hole then reacts with the electron donor, TEA, while the electron is rapidly injected into the cobalt species, leading to reduction of Co^{III} to Co^{II}. We should emphasize that reduction of Co^{III} centers is generally accepted to be one of the first reaction steps in cobaloxime-catalyzed hydrogen evolution, while the presence of high-spin Co^{II} species is likely to play an important role in photocatalytic activity of the whole system.[58] Catalysis taking place at the cobalt metal centres is beyond the scope of this research and thus shown as a dashed arrow in Scheme 3.[59]

In order to demonstrate the feasibility of the proposed mechanism, theoretical[47] and experimental data[48] for the redox potentials of the building blocks of **Co@MOF** are depicted in Scheme 3. The catalytic potential for the cobalt complex is well below the LUMO of the MOF, making the electron injection plausible (ESI†). Fluorescence lifetime spectroscopy revealed that the difference in fluorescence lifetimes of **Co@MOF** composite and the pristine **NH_2-MIL-125(Ti)** was negligible. These observations suggest that the electron transfer from the MOF to the cobalt catalytic centre confirmed by EPR proceeds *via* the so-called 'reductive quenching mechanism'.[60] The mechanism implies that first the photoexcited MOF is quenched (reduced) by an electron donor, whereas the electron-driven transformations involving the cobaloxime species occur after this process is completed (ESI†).

Summarizing, we have designed a 'ship-in-a-bottle' strategy for the synthesis of a **Co@MOF** composite with remarkable photocatalytic performance in hydrogen evolution under visible light illumination. The organometallic Co^{III} species within the catalyst are molecular and highly dispersed over the bulk of the MOF matrix. Most of the characterization techniques applied in this work point at the assembly of cobaloxime **1** within the MOF cavities, however the nature of such **1**-derived cobalt species within **Co@MOF** is different from those found in the homogeneous molecular catalyst.

5. Conclusions

In this work we have reported the facile synthesis of a multifunctional catalyst@MOF composite (**Co@MOF**) through a 'ship-in-a-bottle' approach. The resulting **Co@MOF** composite is a stable material for the efficient photocatalytic production of H_2 from water under visible light illumination. **Co@MOF** can be recycled without loss of activity. Introduction of the molecular Co catalytic active site leads to a 20-fold enhancement in H_2 evolution as compared to the pristine **NH_2-MIL-125(Ti)**, demonstrating the synergy between a stable, photo-active MOF

structure and a **1**-derived Co-based proton reduction catalyst for photocatalysis. The extensive characterization of the composite presented in this work points towards the formation of cobaloxime **1** within the pores of the MOF. However, the exact structure of the cobalt species remains unknown. Being a clear example of multifunctional MOF-based systems, the noble metal free **Co@MOF** catalyst outperforms every MOF based photocatalytic system reported in the literature so far (ESI†). The modular design behind the cooperative action of a photoactive matrix and a catalytically active encapsulated guest will allow for the application of related composites in other photocatalytic applications.

Acknowledgements

The Dutch National Research School Combination Catalysis Controlled by Chemical Design (NRSC-Catalysis), the National Research Initiative BioSolarCells, the Foundation for Fundamental Research on Matter (FOM) and RF President's grant MD-276.2014.3 are gratefully acknowledged for funding this research. Dr P.J. Kooyman of DCT/NCHREM, Delft University of Technology, Delft, The Netherlands, is acknowledged for performing the electron microscopy investigations.

Notes and references

1 N. S. Lewis and D. G. Nocera, *Proc. Natl. Acad. Sci. U. S. A.*, 2006, **103**, 15729–15735.
2 G. A. Olah, G. K. S. Prakash and A. Goeppert, *J. Am. Chem. Soc.*, 2011, **133**, 12881–12898.
3 J. Ronge, T. Bosserez, D. Martel, C. Nervi, L. Boarino, F. Taulelle, G. Decher, S. Bordiga and J. A. Martens, *Chem. Soc. Rev.*, 2014, **43**, 7963–7981.
4 P. Du and R. Eisenberg, *Energy Environ. Sci.*, 2012, **5**, 6012–6021.
5 T. Zhang and W. Lin, *Chem. Soc. Rev.*, 2014, **43**, 5982–5993.
6 A. Fujishima and K. Honda, *Nature*, 1972, **238**, 37–38.
7 W.-J. Ong, L.-L. Tan, S.-P. Chai, S.-T. Yong and A. Mohamed, *Nano Res.*, 2014, **7**, 1528–1547.
8 S. Banerjee, S. C. Pillai, P. Falaras, K. E. O'Shea, J. A. Byrne and D. D. Dionysiou, *J. Phys. Chem. Lett.*, 2014, **5**, 2543–2554.
9 W.-J. Ong, L.-L. Tan, S.-P. Chai, S.-T. Yong and A. R. Mohamed, *ChemSusChem*, 2014, **7**, 690–719.
10 J. Yu, J. Low, W. Xiao, P. Zhou and M. Jaroniec, *J. Am. Chem. Soc.*, 2014, **136**, 8839–8842.
11 J. Zhang, L. Qi, J. Ran, J. Yu and S. Z. Qiao, *Adv. Energy Mater.*, 2014, **4**, DOI: 10.1002/aenm.201301925.
12 J.-L. Wang, C. Wang and W. Lin, *ACS Catal.*, 2012, **2**, 2630–2640.
13 M. A. Nasalevich, M. van der Veen, F. Kapteijn and J. Gascon, *CrystEngComm*, 2014, **16**, 4919–4926.
14 M. G. Goesten, F. Kapteijn and J. Gascon, *CrystEngComm*, 2013, **15**, 9249.
15 C. Wang, D. Liu and W. Lin, *J. Am. Chem. Soc.*, 2013, **135**, 13222–13234.
16 S. Bordiga, C. Lamberti, G. Ricchiardi, L. Regli, F. Bonino, A. Damin, K. P. Lillerud, M. Bjorgen and A. Zecchina, *Chem. Commun.*, 2004, 2300–2301.
17 M. Alvaro, E. Carbonell, B. Ferrer, F. Xamena and H. Garcia, *Chem.–Eur. J.*, 2007, **13**, 5106–5112.
18 F. Xamena, A. Corma and H. Garcia, *J. Phys. Chem. C*, 2007, **111**, 80–85.
19 J. Gascon, M. D. Hernandez-Alonso, A. R. Almeida, G. P. M. van Klink, F. Kapteijn and G. Mul, *ChemSusChem*, 2008, **1**, 981–983.
20 H. Khajavi, J. Gascon, J. M. Schins, L. D. A. Siebbeles and F. Kapteijn, *J. Phys. Chem. C*, 2011, **115**, 12487–12493.
21 J. Gascon, A. Corma, F. Kapteijn and F. X. Llabrés i Xamena, *ACS Catal.*, 2014, **4**, 361–378.
22 M. D. Hernández-Alonso, F. Fresno, S. Suárez and J. M. Coronado, *Energy Environ. Sci.*, 2009, **2**, 1231.
23 C. Wang, K. E. Dekrafft and W. Lin, *J. Am. Chem. Soc.*, 2012, **134**, 7211–7214.
24 Y. Horiuchi, T. Toyao, M. Saito, K. Mochizuki, M. Iwata, H. Higashimura, M. Anpo and M. Matsuoka, *J. Phys. Chem. C*, 2012, **116**, 20848–20853.
25 T. Toyao, M. Saito, Y. Horiuchi, K. Mochizuki, M. Iwata, H. Higashimura and M. Matsuoka, *Catal. Sci. Technol.*, 2013, **3**, 2092–2097.
26 D. Sun, Y. Fu, W. Liu, L. Ye, D. Wang, L. Yang, X. Fu and Z. Li, *Chem.–Eur. J.*, 2013, **19**, 14279–14285.
27 S. Pullen, H. Fei, A. Orthaber, S. M. Cohen and S. Ott, *J. Am. Chem. Soc.*, 2013, **135**, 16997–17003.
28 C. Wang, J. L. Wang and W. Lin, *J. Am. Chem. Soc.*, 2012, **134**, 19895–19908.
29 C. Wang, Z. Xie, K. E. deKrafft and W. Lin, *J. Am. Chem. Soc.*, 2011, **133**, 13445–13454.
30 W. Lubitz, C. J. Winscom, H. Diegruber and R. Möseler, *Z. Naturforsch., A: Phys. Sci.*, 1987, **42**, 970–986.
31 J. Niklas, K. L. Mardis, R. R. Rakhimov, K. L. Mulfort, D. M. Tiede and O. G. Poluektov, *J. Phys. Chem. B*, 2012, **116**, 2943–2957.
32 E. Uhlig and M. Friedrich, *Z. Anorg. Allg. Chem.*, 1966, **343**, 299–307.
33 G. Costa, G. Mestroni and E. de Savorgnani, *Inorg. Chim. Acta*, 1969, **3**, 323–328.
34 J. Juan-Alcaniz, J. Gascon and F. Kapteijn, *J. Mater. Chem.*, 2012, **22**, 10102–10118.
35 S. Vaesen, V. Guillerm, Q. Yang, A. D. Wiersum, B. Marszalek, B. Gil, A. Vimont, M. Daturi, T. Devic, P. L. Llewellyn, C. Serre, G. Maurin and G. De Weireld, *Chem. Commun.*, 2013, **49**, 10082–10084.
36 N. M. Muresan, J. Willkomm, D. Mersch, Y. Vaynzof and E. Reisner, *Angew. Chem., Int. Ed.*, 2012, **51**, 12749–12753.
37 M. A. Nasalevich, M. G. Goesten, T. J. Savenije, F. Kapteijn and J. Gascon, *Chem. Commun.*, 2013, **49**, 10575–10577.
38 J. Huang, K. L. Mulfort, P. Du and L. X. Chen, *J. Am. Chem. Soc.*, 2012, **134**, 16472–16475.
39 J. Säuberlich, O. Brede and D. Beckert, *J. Phys. Chem. A*, 1997, **101**, 5659–5665.
40 H. Drulis, K. Dyrek, K. P. Hoffmann, S. K. Hoffmann and A. Weselucha-Birczynska, *Inorg. Chem.*, 1985, **24**, 4009–4012.

41 J. Long, S. Wang, Z. Ding, S. Wang, Y. Zhou, L. Huang and X. Wang, *Chem. Commun.*, 2012, **48**, 11656–11658.
42 A. Bencini, I. Bertini, G. Canti, D. Gatteschi and C. Luchinat, *J. Inorg. Biochem.*, 1981, **14**, 81–93.
43 F. Jeremias, V. Lozan, S. K. Henninger and C. Janiak, *Dalton Trans.*, 2013, **42**, 15967–15973.
44 S.-N. Kim, J. Kim, H.-Y. Kim, H.-Y. Cho and W.-S. Ahn, *Catal. Today*, 2013, **204**, 85–93.
45 M. De Miguel, F. Ragon, T. Devic, C. Serre, P. Horcajada and H. García, *ChemPhysChem*, 2012, **13**, 3651–3654.
46 C. H. Hendon, D. Tiana, M. Fontecave, C. Sanchez, L. D'arras, C. Sassoye, L. Rozes, C. Mellot-Draznieks and A. Walsh, *J. Am. Chem. Soc.*, 2013, **135**, 10942–10945.
47 K. T. Butler, C. H. Hendon and A. Walsh, *J. Am. Chem. Soc.*, 2014, **136**, 2703–2706.
48 P.-A. Jacques, V. Artero, J. Pécaut and M. Fontecave, *Proc. Natl. Acad. Sci. U. S. A.*, 2009, **106**, 20627–20632.
49 L. A. Berben and J. C. Peters, *Chem. Commun.*, 2010, **46**, 398–400.
50 W. R. McNamara, Z. Han, C.-J. Yin, W. W. Brennessel, P. L. Holland and R. Eisenberg, *Proc. Natl. Acad. Sci. U. S. A.*, 2012, **109**, 15594–15599.
51 L. Tong, R. Zong and R. P. Thummel, *J. Am. Chem. Soc.*, 2014, **136**, 4881–4884.
52 M. Giorgetti, M. Berrettoni, I. Ascone, S. Zamponi, R. Seeber and R. Marassi, *Electrochim. Acta*, 2000, **45**, 4475–4482.
53 M. Krivec, R. Dillert, D. W. Bahnemann, A. Mehle, J. Strancar and G. Drazic, *Phys. Chem. Chem. Phys.*, 2014, **16**, 14867–14873.
54 F. Lakadamyali and E. Reisner, *Chem. Commun.*, 2011, **47**, 1695–1697.
55 F. Lakadamyali, A. Reynal, M. Kato, J. R. Durrant and E. Reisner, *Chem.–Eur. J.*, 2012, **18**, 15464–15475.
56 Y. Ma, X. Wang, Y. Jia, X. Chen, H. Han and C. Li, *Chem. Rev.*, 2014, **114**, 9987–10043.
57 N. Bao, L. Shen, T. Takata and K. Domen, *Chem. Mater.*, 2007, **20**, 110–117.
58 A. Mukherjee, O. Kokhan, J. Huang, J. Niklas, L. X. Chen, D. M. Tiede and K. L. Mulfort, *Phys. Chem. Chem. Phys.*, 2013, **15**, 21070–21076.
59 A. Bhattacharjee, E. S. Andreiadis, M. Chavarot-Kerlidou, M. Fontecave, M. J. Field and V. Artero, *Chem.–Eur. J.*, 2013, **19**, 15166–15174.
60 V. Artero, M. Chavarot-Kerlidou and M. Fontecave, *Angew. Chem., Int. Ed.*, 2011, **50**, 7238–7266.